Volume 2
Number 4
July 2025
Pages 843–1092

RSC Applied Interfaces

rsc.li/RSCApplInter

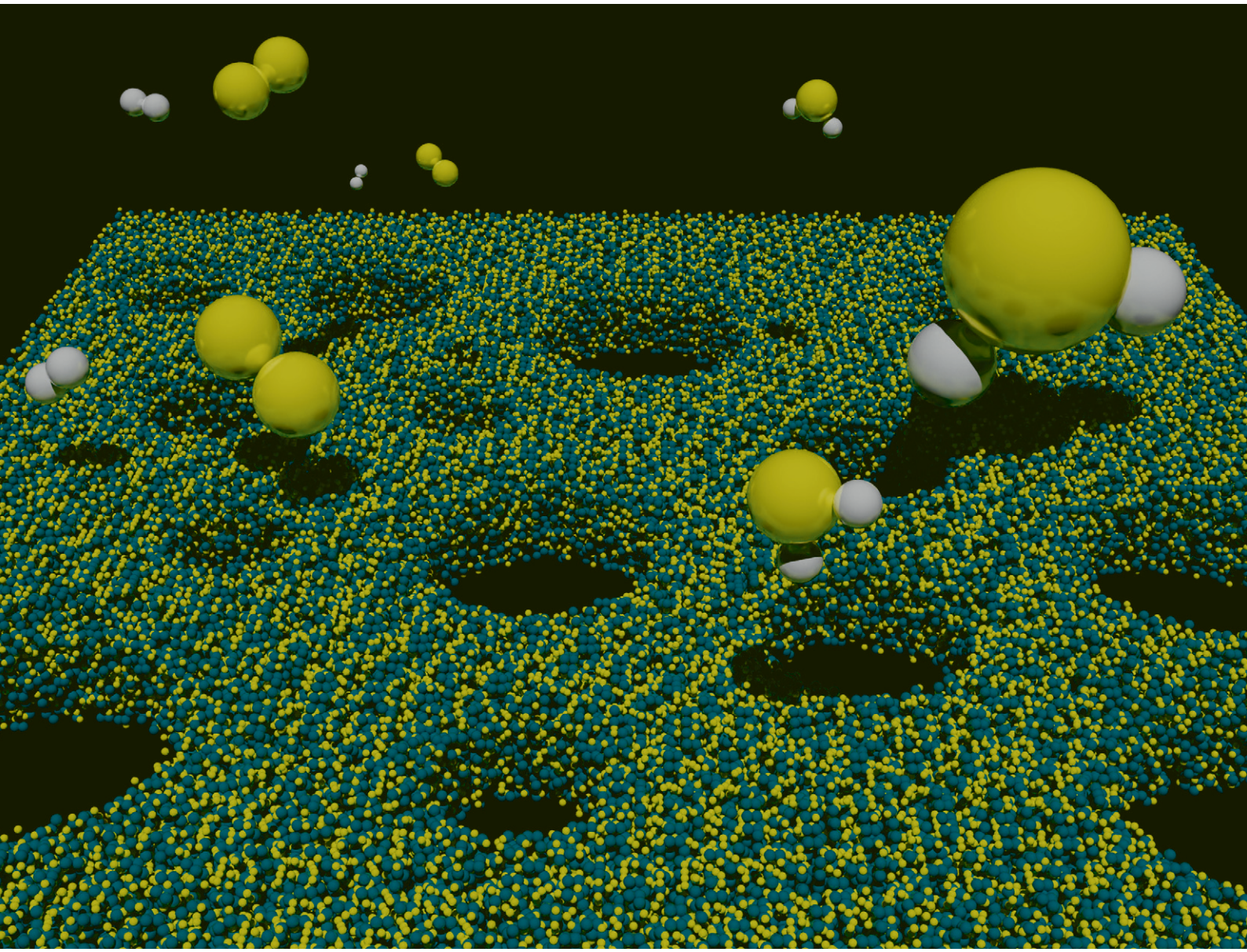

ISSN 2755-3701

ROYAL SOCIETY OF CHEMISTRY

PAPER

Fabiano Bernardi *et al.*

Development of improved MnO_x nanoparticles for the oxygen reduction reaction

RSC Applied Interfaces

ROYAL SOCIETY OF CHEMISTRY

PAPER

View Article Online
View Journal | View Issue

Cite this: *RSC Appl. Interfaces*, 2025, **2**, 922

Development of improved MnO_x nanoparticles for the oxygen reduction reaction†

Marco A. H. Vogt,[a] Alisson S. Thill,[a] Carlos Escudero,[b] Marcus V. Castegnaro[a] and Fabiano Bernardi *[a]

Received 29th March 2025,
Accepted 24th April 2025

DOI: 10.1039/d5lf00090d

rsc.li/RSCApplInter

Manganese oxides (MnO_x) present interesting properties for the oxygen reduction reaction (ORR), but little is known about the influence of their properties on this application. In this work, MnO_x nanostructures were synthesized with different chemical states (MnO_2 and Mn_2O_3) with or without pore ordering. The samples were used in the ORR at 500 °C before and after reduction treatment at this same temperature. The results point to an improved performance of Mn_3O_4 in comparison with MnO_2 or Mn_2O_3 compounds. These results are further verified with kinetic Monte Carlo simulations. Furthermore, it is demonstrated that the samples without pore ordering present better results towards H_2O production. This means that pore ordering is not important for this reaction, which simplifies the future design of MnO_x nanostructures for ORR application.

Introduction

Manganese oxide (MnO_x) presents a rich chemistry with distinct Mn oxidation states, namely +2, +3, +4, +6, and +7, besides different crystal structures, both dependent on the x value.[1] Additionally, MnO_x may exhibit mixed valence states like Mn(II, III) (Mn_3O_4), where different Mn ions have different oxidation states. This phenomenon arises from charge transfer and electron delocalization between adjacent Mn sites, resulting in a distribution of oxidation states across the material.[2] The diversity of MnO_x electronic and structural properties allows a wide range of applications, such as in molecular adsorption,[3] supercapacitors,[4] ozone decomposition,[5] aerobic oxidation of amines,[6] nitric oxide reduction,[7] oligomerization of methane,[8] and photocatalytic oxidation of organic pollutants.[9] In particular, MnO_x presents high O storage and release capacity and exhibits high mobility of the O ions. These characteristics are ideal for applications like the ORR (oxygen reduction reaction),[10] where MnO_x was recently used.[11]

The ORR has been extensively investigated due to its crucial role in energy conversion and storage systems such as fuel cells and metal–air batteries.[12] The most widely used material in electrodes for the ORR is still Pt, since it matches the required compromise between a low energy barrier for O_2 dissociative adsorption and low affinity to the reactive species formed during the reaction. However, Pt is an expensive and scarce metal, and Pt electrodes suffer from leaching and poisoning in practical applications,[13] thus limiting their performance. Alternative materials have been used in the literature for this purpose.[14,15] Metal oxides have emerged as promising substitutes for noble metal-based electrocatalysts.[16] Among them, MnO_x has been studied for the ORR and has already been shown to have a catalytic activity close to that of Pt.[11] These characteristics are already enough to consider MnO_x as a potential candidate for new applications in catalysis. Furthermore, there is the intrinsic cost-effective production associated with MnO_x that makes this material even more interesting, in particular for replacing Pt in the ORR.

Despite that, there are many open questions about the influence of the electronic and structural properties of MnO_x on the ORR activity. The influence of the Mn oxidation state was investigated for epitaxial films of a perovskite-type structure ($AMnO_x$ with A representing a transition metal), where the maximum ORR activity was achieved for a Mn oxidation state close to +3.5,[11] but this system is far away from that of MnO_x nanostructures. In parallel, it is missing a deeper fundamental understanding of the atomic processes involving phase transitions between different Mn oxide phases that may occur during the ORR. This understanding would lead also to the design of improved routes to achieve the ideal oxidation state of the MnO_x system. Regarding the structural properties, metal oxides usually present a porous structure, but the influence of pore ordering of MnO_x on the ORR activity was not studied. Typically, ordered porous metal oxides present higher catalytic activity than disordered

[a] *Programa de Pós Graduação em Física, Instituto de Física, Universidade Federal do Rio Grande do Sul (UFRGS), Porto Alegre, RS, Brazil.*
E-mail: bernardi@if.ufrgs.br
[b] *ALBA Synchrotron Light Source, Cerdanyola del Vallès, Barcelona, Spain*

† Electronic supplementary information (ESI) available. See DOI: https://doi.org/10.1039/d5lf00090d

porous structures due to the improved mass transport.[17,18] However, Weller *et al.* demonstrated that $CsTaWO_6$ presents the opposite behavior for the photocatalytic hydrogen evolution reaction where the low long-range order case presents improved performance over the high one due to the better connectivity of pores, which facilitates the reaction.[19] For the ORR, the effect of pore ordering on the catalytic activity is ambiguous since reports show good performance for both ordered and disordered systems.[20] This is still an important open question that may strongly impact the use of metal oxides, in particular, MnO_x, in the ORR. The absence of the need for pore ordering would simplify the synthesis procedure and speed up the use of MnO_x for the ORR.

In view of the above, the main goal of this study is to elucidate the atomic mechanism of phase transitions in ordered and disordered porous MnO_x nanostructures, and the influence of pore ordering and the oxidation state of Mn on their reactivity towards the ORR. Understanding all these factors will enable us to find the best routes for achieving the improved oxidation state and pore ordering of MnO_x nanostructures for the ORR.

Experimental and theoretical procedure

The porous MnO_x nanostructures were obtained using SBA-15 as the sacrificial template. The disordered nanostructures were obtained following the method reported by Wang *et al.*[21] For the synthesis, 0.5 g of SBA-15 was added to 8.4 mL of absolute ethanol and stirred at 0 °C for 15 minutes. Then, 1.4 mL of a 50 wt% $Mn(NO_3)_2{\cdot}xH_2O$ solution was added to this suspension. The mixture was continuously stirred for 4 h. After that, 30 mL of a 2 M ammonia carbonate solution was added to raise the pH to approximately 10. The reason for elevating the pH is to decrease the solubility of the solution and favor the precipitation of the Mn salt inside the SBA-15 pores, thus creating many seeds of $Mn(NO_3)_2{\cdot}xH_2O$.[22] After 5 cycles of centrifugation and washing with deionized water, the resulting solid passed through a calcination process at 400 °C for 1 h. To remove the template, the powder was added to a 2 M NaOH solution, heated, and kept at boiling temperature under reflux conditions for 30 min. The final disordered mesoporous MnO_2 sample was obtained by drying it in a vacuum at $p = 8.5 \times 10^{-4}$ mbar and room temperature for 4 h. Hereafter, this sample is labeled D-MnO_2. A modification of the synthesis described was conducted by changing the temperature of the calcination step to 650 °C while keeping the same time (3 h), aiming to change the oxidation state of Mn. This sample is labeled D-Mn_2O_3.

Regarding the ordered nanostructures, a variation of the method for disordered nanostructures was employed following the procedure described elsewhere.[23] In this case, after impregnating SBA-15 with $Mn(NO_3)_2{\cdot}xH_2O$, it was dried at 80 °C for 12 h, and then a calcination process in two steps was carried out. The calcination starts at 200 °C for 6 h and it continues at 400 °C for 6 h more. It is known from the literature[24] that the oxidation from Mn(II) to Mn (IV) starts at 200 °C, so the calcination step at this temperature produces Mn(IV) that crystallizes in the MnO_2 phase.[25] The obtained sample is labeled O-MnO_2.

The sample morphology was investigated by transmission electron microscopy (TEM). The TEM images were obtained at CM-UFMG using a Tecnai G2-12 microscope working at 120 kV. The powder was dispersed in isopropanol by ultrasonication for 20 min, and a drop of the solution was placed over a carbon coated Cu grid. The nanoparticle sizes were estimated using the average Feret diameter, which was manually measured using ImageJ software (2019 version) for isolated and/or easily distinguishable particles.

Small angle X-ray scattering (SAXS) measurements were conducted using Nano-inXider (Xenocs) equipment at CNANO-UFRGS. Around 10 mg of the sample powder was placed in a solid sample holder and sealed with Kapton tape. The SAXS patterns were acquired with a Cu Kα X-ray source and a Dectris Pilatus 3 detector. The measurements were performed in transmission mode with a 2θ range from 0.00° to 5.25° and 60 s exposure time for each scan. The final SAXS pattern was the result of an average of 60 scans. The conversion of symmetric 2D SAXS data to 1D data and the average between multiple scans were made using FOXTROT software.

The morphological, structural, and electronic properties of the as-prepared samples were investigated. N_2 adsorption–desorption isotherm measurements of the samples were acquired at the boiling point of liquid nitrogen, using Tristar II 3020 Micromeritics Instrument Corporation equipment at CA-IQ-UFRGS. The samples were previously degassed for 12 h under vacuum at 120 °C. The specific surface areas were determined by the BET (Brunauer, Emmett and Teller) multipoint technique, and the pore size distribution was obtained by using the BJH (Barrett, Joyner and Halenda) method.

X-ray diffraction (XRD) measurements were performed at CNANO-UFRGS using a Rigaku Ultima IV diffractometer and a Cu Kα X-ray source (λ = 1.5406 Å). The data were collected for the 2θ range from 20° to 80°, using a 0.05° s^{-1} speed. The inorganic crystal structure database (ICSD) was used for indexing the XRD patterns. The Rietveld refinement of the XRD patterns was performed with the FullProf Suite software (July/2017 version). The instrument resolution file was obtained by refining the XRD pattern of the SiO_2 standard ($P3221$ space group with a trigonal crystal structure). The refinement was performed using a Thompson–Cox–Hasting pseudo-Voigt convoluted with axial divergence asymmetry[26] as the profile function. The V and W parameters were fixed to 0 to analyze the XRD patterns of the nanoparticles. The background was adjusted using linear interpolation with 30 experimental points. The transparency parameter was also restricted to positive values.

X-ray photoelectron spectroscopy (XPS) measurements were used to probe the chemical components at the surface

of the MnO_x nanostructures. The experiments were conducted at LAMAS-UFRGS using an Al Kα X-ray source ($h\nu$ = 1486.6 eV). The XPS data were collected at room temperature using an Omicron Sphere analyzer. For the long scan region, the pass energy was set to 50 eV and the data were collected using a step size of 1 eV and an acquisition time of 0.2 s. The high resolution spectra at Mn 2p, O 1s, and C 1s regions were collected with a 0.2 eV step size, an acquisition time of 0.2 s, and a 20 eV pass energy. The XPS spectra were analyzed using the CasaXPS software. The high resolution spectra were fitted using a Shirley-type background and symmetric Gaussian–Lorentzian function with 30% Lorentzian contribution. The adventitious carbon component at 284.5 eV was used for the correction of charging effects.[27] For the fitting, the FWHM and the relative binding energy of each component were constrained to the same value in all samples. The exception was in the O 1s region where a variation of 0.5 eV in the relative binding energy was accepted between the samples. The area ratio and energy spacing between Mn $2p_{3/2}$ and Mn $2p_{1/2}$ energy levels were fixed to reported values.[27]

In situ time-resolved XANES measurements were performed at the BL16-NOTOS beamline at the ALBA Synchrotron in transmission mode at the Mn K edge (6539 eV). For the measurements, about 5 mg of the sample powder was mixed with 45 mg of boron nitride, and this mixture was compacted to produce homogeneous pellets with a diameter of 13 mm. The *in situ* time-resolved XANES measurements were performed with a 0.33 eV energy step and 0.12 s per point integration time. For the measurements, the sample was initially exposed to 30 mL min^{-1} of 20% O_2 + 80% He atmosphere at room temperature. Afterward, the sample was heated to 500 °C at a 10 °C min^{-1} rate in the same oxidant atmosphere. When reaching 500 °C, the flow was decreased to 5 mL min^{-1} of 20% O_2 + 80% He and 50 mL min^{-1} of 4% H_2 + 96% He atmosphere was added, which corresponds to the ORR conditions. The sample was exposed to ORR conditions for 30 min. After this, the O_2 atmosphere was removed and the sample was left exposed to 50 mL min^{-1} of 4% H_2 + 96% He for 20 min. Then the sample was exposed again to the ORR atmosphere for 30 min. At the end, the sample was cooled to RT under a He atmosphere. *In situ* time-resolved XANES measurements were acquired continuously throughout the entire process. A mass spectrometer (CIRRUS 3XD, MKS) was coupled to the reactor outlet to analyze the products of the ORR. *In situ* XRD patterns were also measured with $h\nu$ = 13 keV (λ = 0.95 Å) in a transmission mode (Debye–Scherrer) geometry using a 6 module single-photon-counting silicon microstrip Mythen-I detector (PSI-DECTRIS) in the 2θ range from 5° to 45° before and after each step described above.

The kinetic Monte Carlo (kMC) simulation was applied to investigate the kinetics of the ORR at the MnO_x surface. This method enables the modeling of solid–gas reactions to study the influence of temperature, gas pressure, and the oxidation state on the catalytic activity. The Zacros package[28] was used for kMC simulation of the non-electrolytic ORR for the β-MnO_2 (110) and Mn_3O_4 (110) surfaces. For both β-MnO_2 and Mn_3O_4, the (110) surface was used because it is the most energetically favorable surface and it should represent the typical case in an application.[29] The ORR was simulated with a 2 : 1 H_2/O_2 atmosphere in the temperature range from 427 °C to 927 °C using reaction times from 50 μs to 2000 s. The longer reaction times were used exclusively for the β-MnO_2 (110) surface due to the need for extracting reliable results at low temperatures where the activity is significantly reduced. The total gas pressure was kept constant at 1 bar. Detailed information about the cell mode, catalytic sites, and reaction paths are shown in Fig. S1 and S2 of the ESI† along with the kinetic equations used in the simulation.

Results and discussion

The morphology of the nanostructures synthesized was probed by TEM and the representative images of each sample are shown in Fig. 1(a)–(f). Fig. 1(a)–(c) show the existence of big structures formed by small nanoparticles in the inner part. These big structures have an irregular, rod and spherical like shape for the O-MnO_2, D-MnO_2, and D-Mn_2O_3 samples, respectively. The nanoparticles forming these big structures are nearly spherical with a diameter of *ca.* 15 nm in all cases, as shown in Fig. 1(d)–(f). The particular case of the O-MnO_2 sample presents an additional feature. The big structures exhibit nanoparticles aligned forming stripes with an ordered porous structure existing between the stripes. The same alignment is not observed for the disordered samples.

The existence of an ordered pore structure in the O-MnO_2 sample is confirmed by SAXS measurements that are shown in Fig. 2(a). The SAXS pattern of the O-MnO_2 sample is the only case with a clear structure factor, in agreement with the feature observed in the TEM images. Considering this, two mean pore sizes were determined from the peak positions in the SAXS pattern, around 6 nm and 10 nm, consistent with a pore ordering in the mesoporous regime. Fig. S3 of the ESI† shows the N_2 adsorption–desorption isotherms and the corresponding BJH pore size distributions, while the surface area, pore volume, and pore size are shown in Table S1 of the ESI.† In all cases, the presence of pores in the mesoporous regime is clear. The D-Mn_2O_3 sample presents the highest surface area value, while D-MnO_2 shows the biggest pore volume and pore size. In particular, the O-MnO_2 sample presents an average pore diameter consistent with the findings from SAXS measurements.

Fig. 2(b) shows the XRD patterns and the indexing for all cases. Both O-MnO_2 and D-MnO_2 samples show ε-MnO_2 (ICSD 29661) and β-MnO_2 (ICSD 393) as the main phases. The phases are hardly distinguishable, and each one cannot be discarded, but in the O-MnO_2 sample, the combination of both phases improves the χ^2 factor of Rietveld refinement from 2.7 to 2.2. The XRD pattern of the D-MnO_2 sample was not refined due to the poor crystallinity of the sample. The O-MnO_2 sample presents another crystalline phase of γ-MnO_2 (ICSD 78331), which may also be present in the D-MnO_2 sample in small amounts, considering the XRD pattern

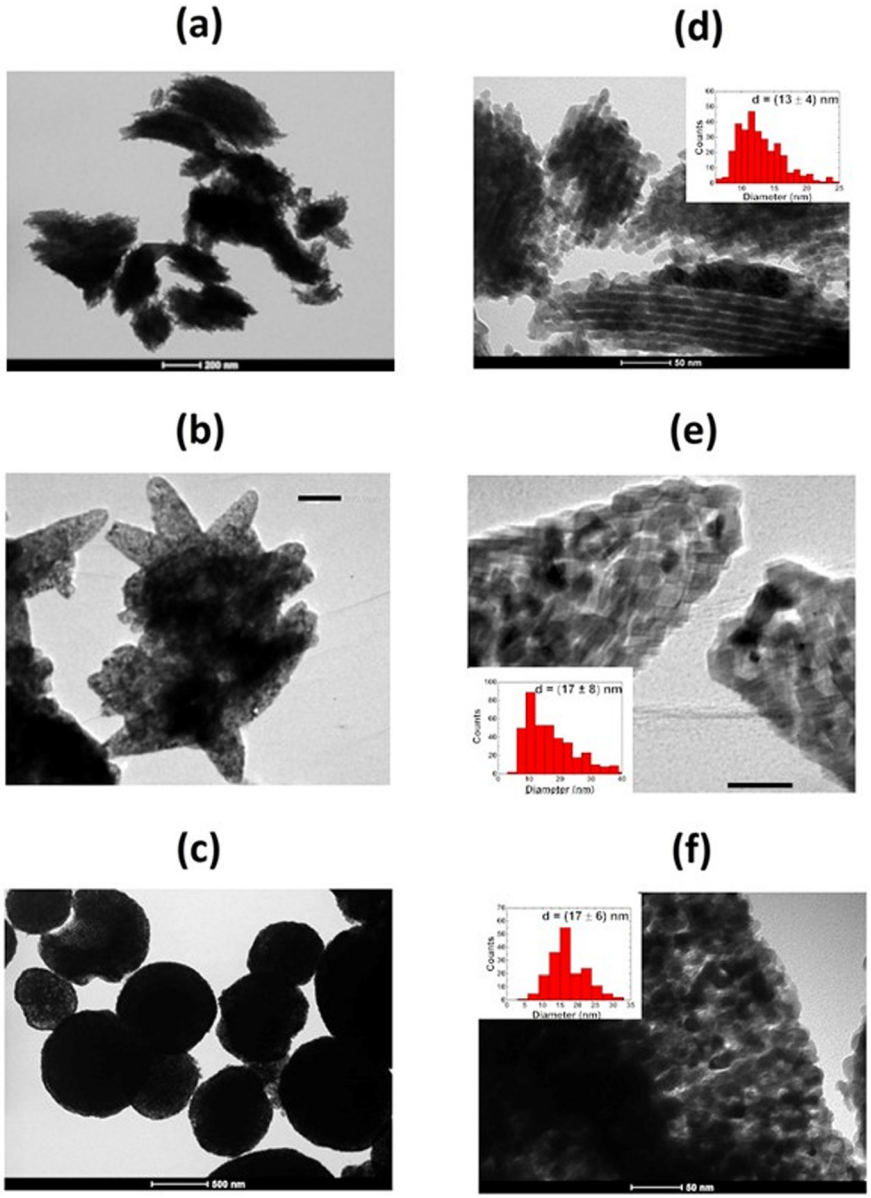

Fig. 1 Typical TEM images of (a and d) O-MnO_2, (b and e) D-MnO_2 and (c and f) D-Mn_2O_3 samples at distinct magnifications and the respective histograms of their size distribution.

shown. It is known that the γ-MnO_2 phase is stable during the calcination process for $T < 350$ °C, while for higher temperatures, there is a phase transition to the β-MnO_2 phase.[25] In this case, a small fraction of the γ-MnO_2 phase remains after the calcination step. The D-Mn_2O_3 sample presents only the Mn_2O_3 phase (ICSD 9091), which confirms the oxidation state of Mn(III). Table S2 of the ESI† shows the Rietveld refinement results found. The crystallite sizes of the main phases are around 20 nm, in agreement with the TEM results since XRD is more sensitive to bigger crystallites.[30]

Fig. 2(c) shows the Mn 2p XPS spectra of the samples. For all cases, two chemical components are shown at 641.6 eV and 642.6 eV, corresponding to Mn(III) and Mn(IV) oxidation states, respectively.[23] The Mn(III) oxidation state in samples with the main phase of MnO_2 comes from the existence of O vacancies at the surface. On the other hand, the Mn(IV) oxidation state in the D-Mn_2O_3 sample is formed due to air exposure and the formation of localized bonds at the surface and is therefore not identified by XRD. Both features are usual characteristics of metal oxides including MnO_x.[9] The XPS results indicate clear differences in the oxidation state of Mn at the sample surface. The main difference comes from the higher Mn(III)/Mn(IV) ratio of the O-MnO_2 sample in comparison with the other cases. The higher relative amount of Mn(III) in the ordered sample is related to the calcination step at 200 °C during the synthesis, which was performed only in this case. Since it is well known that Mn(II) transforms into Mn(IV) at this temperature,[24] the Mn(III) oxidation state should be produced as well and it gives a relatively high concentration of Mn(III) for the O-MnO_2 sample. Fig. S4 of the ESI† shows the O 1s XPS measurements of the

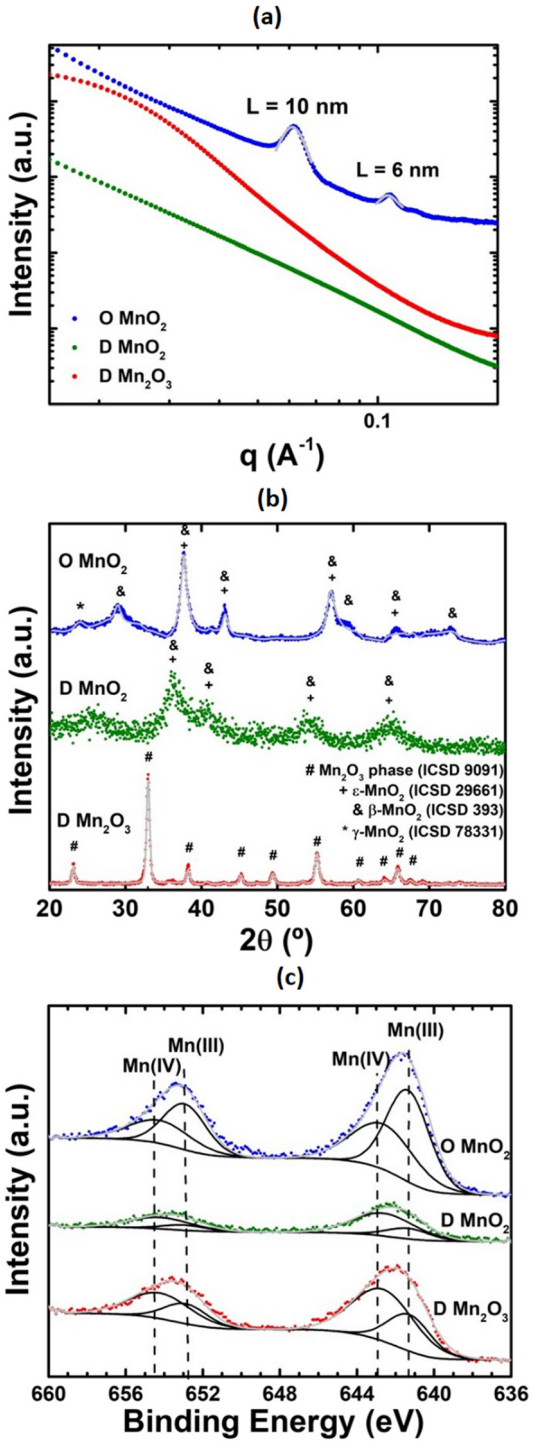

Fig. 2 (a) SAXS patterns, (b) XRD patterns with the corresponding Rietveld refinement result, and (c) Mn 2p XPS spectra of O-MnO_2, D-MnO_2, and D-Mn_2O_3 samples.

samples. The O 1s XPS region presents three components, namely MnO_x, OH, and C–O groups.[31] The MnO_x component is slightly shifted to lower binding energies in the MnO_2 sample, which is consistent with the higher Mn(III)/Mn(IV) ratio in this sample since the O 1s region of Mn_2O_3 presents smaller binding energy than MnO_2.[32,33]

Fig. 3(a)–(c) show the *in situ* short XRD measurements before the ORR at 500 °C in an O_2 atmosphere and a H_2 atmosphere. It is possible to observe the same Bragg reflections under an O_2 atmosphere at 500 °C as those observed in the as-prepared case for the O-MnO_2 and D-Mn_2O_3 samples, as expected. The reduction process induces a phase transition to Mn_3O_4 (ICSD 33327) in all the samples with the appearance of the characteristic Bragg reflections. The D-MnO_2 and O-MnO_2 samples reduce almost directly to Mn_3O_4 without the presence of the Mn_2O_3 phase during the reduction process at 500 °C. On the other hand, after the reduction treatment, the D-Mn_2O_3 sample was not fully reduced to Mn_3O_4 even for a much longer period of reduction treatment (200 minutes against 20 minutes of the other samples). This is due to the high activation energy associated with the transformation from Mn_2O_3 to Mn_3O_4. This means that the Mn_3O_4 phase is reachable in an easier way starting from the MnO_2 phase instead of the Mn_2O_3 phase, and this gives an important hint whether the Mn_3O_4 phase is the desired one for some applications. Since the reduction treatment represents the activation step of a catalyst, synthesizing MnO_2 nanoparticles would be more interesting than Mn_2O_3 nanoparticles for achieving the Mn_3O_4 final state. The D-Mn_2O_3 sample was chosen to study a possible change in the morphology of the nanoparticles after the thermal treatment since this sample was exposed to the longest reduction period, but no significant changes were observed by TEM (Fig. S5 of the ESI†).

The time evolution of the Mn oxidation state during thermal treatment was determined by *in situ* time-resolved XANES measurements at the Mn K edge. No changes in the XANES spectra, thus in the Mn oxidation state, were observed until reaching 500 °C under an O_2 atmosphere (not shown here), in accordance to the *in situ* time-resolved XRD measurements. The picture quickly changes after H_2 insertion at 500 °C. Fig. 3(d) shows a typical *in situ* time-resolved XANES measurement during the reduction treatment of the O-MnO_2 sample. It is possible to observe that the fingerprints of the XANES spectra change dramatically in a short period of around 12 minutes, whose features correspond to a change from MnO_2 to Mn_3O_4. The XANES spectra are well adjusted by a linear combination of XANES spectra from MnO_2 and Mn_3O_4 standards, as depicted in Fig. S6 of the ESI.† Fig. 3(e) shows the time evolution of the Mn_3O_4 fraction for each sample. The D-MnO_2 and O-MnO_2 samples present a significant Mn_3O_4 fraction (~0.4) at the beginning of the reduction process due to the ORR before the reduction treatment. It is also possible to observe that both samples are reduced much faster than the D-Mn_2O_3 sample, thus indicating that it is hard to achieve the Mn_3O_4 compound starting from Mn_2O_3, as observed in the *in situ* time-resolved XRD measurements. Even after 200 min under a H_2 atmosphere at 500 °C, the D-Mn_2O_3 sample reaches equilibrium and it is not able to have more than 60% Mn_3O_4. For the MnO_2 compound, the O-MnO_2 sample is reduced faster than the D-MnO_2 sample. This difference may be associated with different reduction mechanisms in the samples.

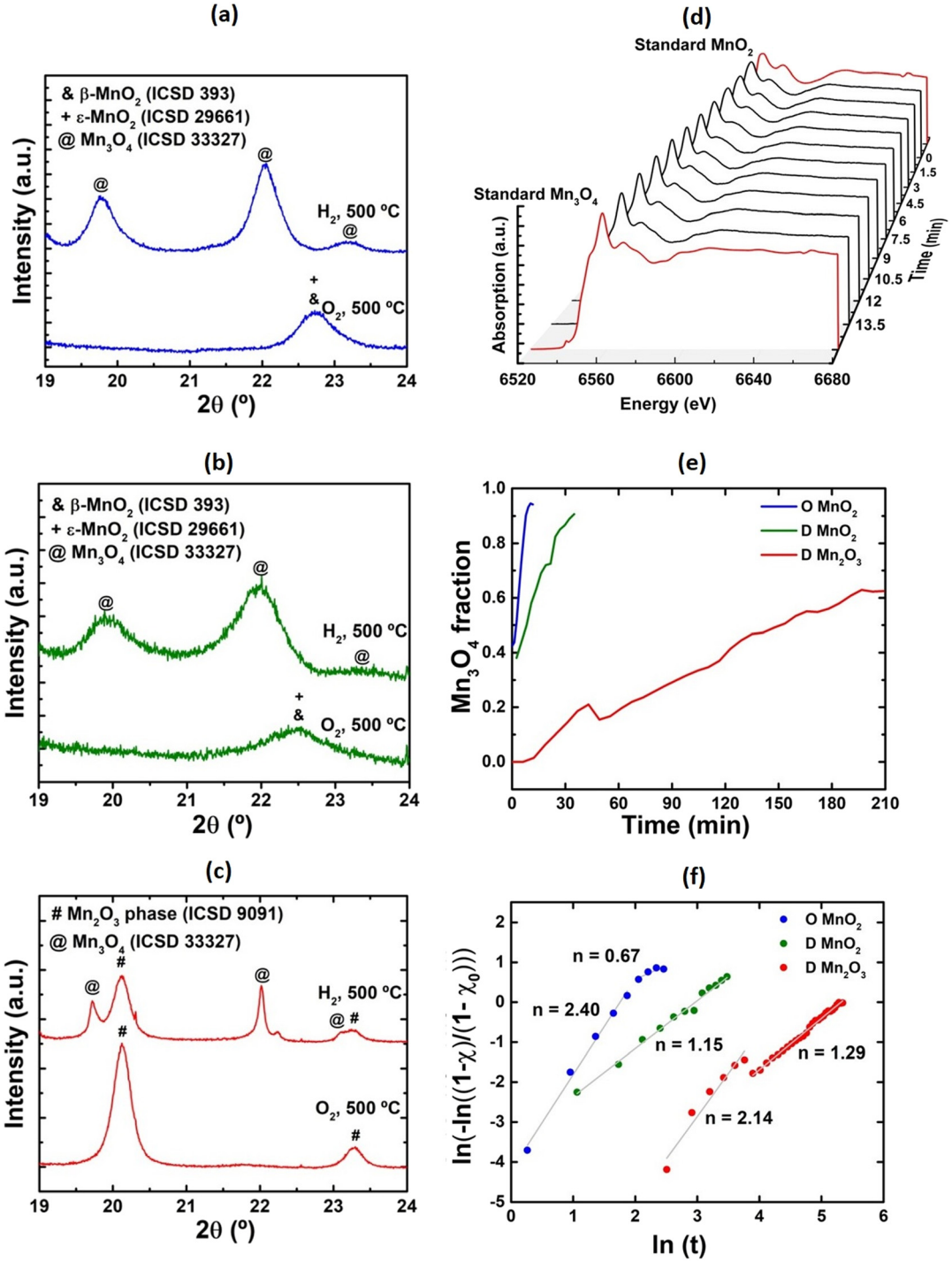

Fig. 3 Short *in situ* XRD measurements of (a) O-MnO_2, (b) D-MnO_2, and (c) D-Mn_2O_3 nanoparticles under an O_2 and H_2 atmosphere at 500 °C. (d) Typical *in situ* time-resolved XANES spectra at the Mn K edge during reduction treatment for the O-MnO_2 sample. (e) Time evolution of the Mn_3O_4 fraction during the reduction process in a H_2 atmosphere. (f) Graph of $\ln(-\ln((1-\chi)/(1-\chi_0)))$ as a function of $\ln(t)$ for O-MnO_2, D-MnO_2 and D-Mn_2O_3 samples. The points represent the experimental data obtained from *in situ* time-resolved XANES analysis and the straight line shows the best fit found.

Avrami's theory[34,35] was employed to study in greater detail the kinetics of phase transformation through the determination of the reduction mechanism. The determination of Avrami's coefficient (n) allows the discovery of the dimension of phase transition.[36] Fig. 4(c) shows the $\ln(-\ln(1-\chi_t)/(1-\chi_0))$ as a function of $\ln(t)$, where χ_t is the Mn_3O_4 fraction at a given time t, and χ_0 is the initial Mn_3O_4 fraction of the sample. It is possible to observe two linear regions for the O-MnO_2 and D-Mn_2O_3 samples, which indicates that the nature of the mechanism changes during the reduction process for these

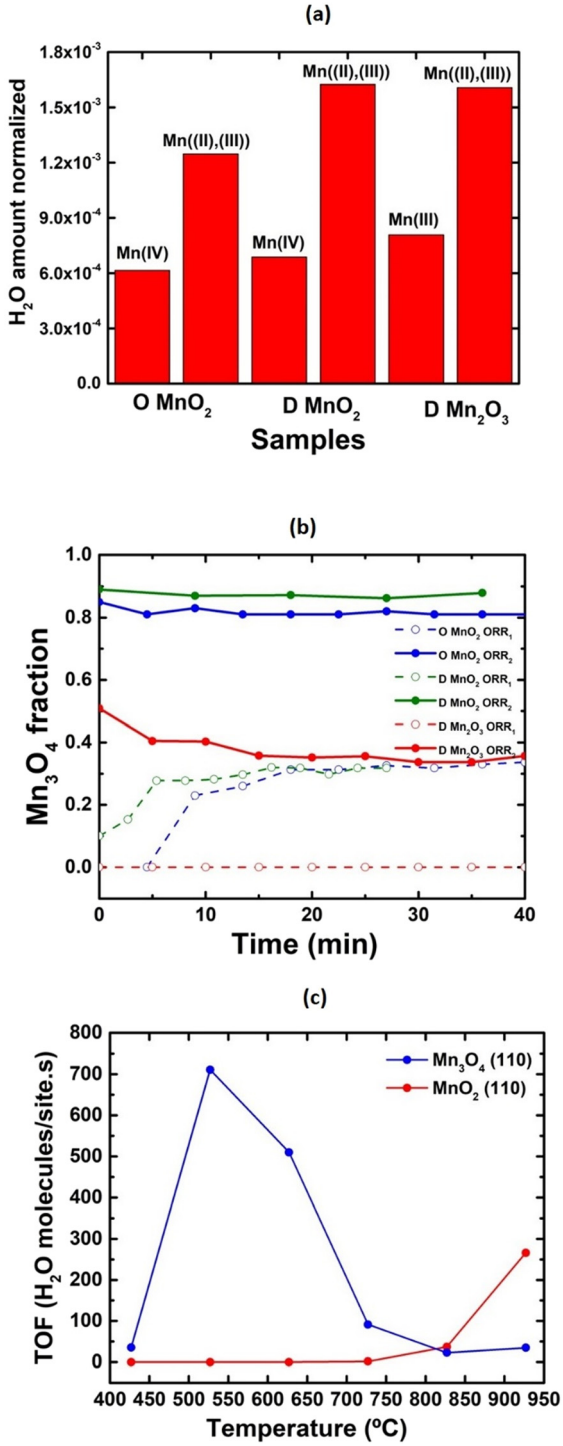

Fig. 4 (a) H_2O amount normalized by the surface area before (left) and after (right) reduction treatment for each sample. (b) Time evolution of the Mn_3O_4 fraction during the ORR before (open circles) and after (solid circles) reduction treatment. (c) ORR turnover frequency as a function of temperature for β-MnO_2 (110) and Mn_3O_4 (110) surfaces. Obtained from kMC simulations.

samples. The angular coefficient of each straight line is Avrami's coefficient n, where $n < 2$ for a phase transition in 1D, $2 < n < 3$ for 2D, and $n > 3$ for a 3D phase transition. It is possible to observe that the D-MnO_2 sample presents a single 1D mechanism of phase transformation in the full reduction treatment, but the O-MnO_2 sample changes from the 2D to 1D mechanism at the end of the process. This means that pore ordering has a strong influence on the nature of the reduction mechanism, thus influencing the O mobility of the sample which is important for ORR application. Moreover, the initial oxidation state also has an influence on the nature of the mechanism since the D-Mn_2O_3 sample starts the phase transition in 2D and readily changes to 1D.

Mass spectrometry measurements were performed during the ORR before and after reduction treatment at 500 °C. Fig. 4(a) shows a comparison of the H_2O production normalized by the surface area from BET analysis for the different samples before (left) and after (right) reduction treatment. In this way, it is possible to compare the efficiency of the catalytically active sites existing in each sample for the ORR, independent of the amount of catalytically active sites (surface area). The main oxidation state of each case is also indicated. Firstly, it is clear that the reactivity towards H_2O production is higher for Mn_3O_4 than for MnO_2 or Mn_2O_3 compounds in all samples, independent of the presence or absence of pore ordering. The MnO_2 and Mn_2O_3 compounds present almost the same small reactivity (considering the uncertainty) and it is not possible to conclude about the influence of pore ordering using the reactivity of these compositions. However, the comparison of the samples with Mn_3O_4 as the main compound presents a clear trend of improvement of the reactivity in the ORR for the disordered samples as compared to the ordered one. The D-MnO_2 and O-MnO_2 samples present almost the same oxidation state, but the improved activity of the D-MnO_2 sample comes from the bigger pore volume and pore size (see Table S1†), which are known as important characteristics for improving mass transport.[20,37] On the other hand, both D-MnO_2 and D-Mn_2O_3 samples produce the same amount of H_2O normalized, but the Mn_3O_4 fraction is higher for D-MnO_2 (0.9) as compared to the D-Mn_2O_3 (0.6) sample, as determined in Fig. 3(e). The smaller amount of Mn_3O_4 is probably compensated by the better pore connectivity in this sample. It is expected that the pore connectivity is better for structures presenting higher surface area and smaller pore volume and pore size. Considering this, the similar activity between these two samples can be understood. The pore connectivity improves the O_2 and H_2 diffusion in the sample, thus achieving high efficiency for H_2O production, as observed in the literature for the photocatalytic hydrogen production with $CsTaWO_6$.[19] These results demonstrate the possibility of using simple routes for enhancing the efficiency of MnO_x nanostructures for the ORR since complex procedures dedicated to producing pore ordering are not needed in this case.

Fig. 4(b) shows the time evolution of the Mn_3O_4 fraction during the ORR from *in situ* XANES measurements before (open circles) and after (solid circles) reduction treatment at 500 °C. Before reduction, the O-MnO_2 and D-MnO_2 samples start to transform from MnO_2 to Mn_3O_4 quickly after insertion of the $2H_2 + O_2$ atmosphere. On the other hand, the D-Mn_2O_3 sample does not change the oxidation state under

exposure to the same atmosphere because Mn_2O_3 is hardly reduced to Mn_3O_4 (see Fig. 3(e)). After reduction treatment, both O-MnO_2 and D-MnO_2 samples keep the same oxidation state of Mn_3O_4 during the ORR. A small oxidation from Mn_3O_4 to Mn_2O_3 at the beginning of the ORR is achieved for the D-Mn_2O_3 sample. It influences the reactivity of this sample but, even so, the pore connectivity helps to obtain a good reactivity towards H_2O formation.

Fig. 4(c) shows a comparison of the TOF values as a function of the temperature for the β-MnO_2 (110) and Mn_3O_4 (110) surfaces calculated by kMC. Interestingly, both surfaces present a completely distinct trend with the temperature. For the β-MnO_2 (110) surface, the activity increases exponentially with the temperature as a result of the higher amount of available thermal energy, as expected. This surface starts to be effectively active for temperatures higher than 900 °C. The picture strongly changes for the Mn_3O_4 (110) surface. In this case, the TOF value reaches a maximum at around 500 °C and it decreases for higher temperatures. This occurs because, at high temperatures, O vacancies start to form at the Mn_3O_4 (110) surface in opposition to the MnO_2 (110) surface (not shown here), and they act as traps of the intermediate products. Furthermore, the Mn_3O_4 (110) surface is much more active for the ORR than β-MnO_2 (110), and it presents a theoretical TOF value of around 700 molecules per site. The comparison with other materials used for the ORR in the literature is not direct since there is no electrical potential used here, but Pt/C at 60 °C in the electrochemical reaction reaches a TOF value between 10^{-3} and 100 molecules per site, depending on the potential applied to the system.[38] The activation energy (E_a) for the ORR over the β-MnO_2 (110) and Mn_3O_4 (110) surfaces was extracted from the dependence of the TOF values on the temperature. The E_a values obtained were 289 kJ mol^{-1} and 139 kJ mol^{-1} for the β-MnO_2 (110) and Mn_3O_4 (110) surfaces, respectively. The Mn_3O_4 (110) surface shows an activation energy less than half of the β-MnO_2 (110) surface case. For comparison purposes, Pt (100) and Pt (111) surfaces present activation energies of 77.19 kJ mol^{-1} and 76.23 kJ mol^{-1}, respectively.[39] The catalytic behavior of the Mn_3O_4 (110) surface is theoretically comparable with the Pt case, showing that this surface is highly promising for technological applications since Mn_3O_4 is much cheaper than the Pt material. This added to the absence of complex procedures for pore ordering, opening new possibilities for the future of energy conversion and storage systems. The system needs to be tested in the electrochemical reaction, but the present findings already show a great opportunity to improve the ORR through the use of Mn_3O_4 without pore ordering that is synthesized without complex procedures.

Conclusions

In this study, three different approaches were used to synthesize MnO_x nanostructures using SBA-15 as a sacrificial template. The different synthesis procedures led to different pore ordering and Mn oxidation states. The Mn_3O_4 compound presents better reactivity towards H_2O production in the ORR. The best route to achieve this compound is starting the reduction from MnO_2 instead of Mn_2O_3. The pore ordering does not play a key role in the ORR since the samples with disordered pores present better connectivity between the pores and this improves the reactivity towards H_2O formation. These results contribute to the future design of improved MnO_x nanostructures for the ORR.

Data availability

The data supporting this article have been included as part of the ESI.†

Conflicts of interest

There are no conflicts to declare.

Acknowledgements

This study was funded by CNPq (project number 310142/2021-0), FINEP (project number 01.22.0231.00), FAPERGS (project number 23/2551-0000177-2), and CAPES (finance code 001). C. E. acknowledges the MICINN-FEDER funding through the PID2021-124572OB-C33 grant. M. A. H. V. thanks CAPES for the research grant. A. S. T. and F. B. thank the CNPq for the research grant. The authors thank Prof. Anderson J. Schwanke for the N_2 adsorption–desorption isotherms analysis. The authors also thank CNANO, LAMAS, CM-UFMG, and ALBA for the use of the infrastructure.

References

1 Y. Wang, H. Arandiyan, J. Scott, A. Bagheri and R. Amal, *J. Mater. Chem. A*, 2017, **5**, 8825–8846.
2 G. S. Gautam and E. A. Carter, *Phys. Rev. Mater.*, 2018, **2**, 95401–95415.
3 J. Fei, Y. Cui, X. Yan, W. Qi, Y. Yang, K. Wang, Q. He and J. Li, *Adv. Mater.*, 2008, **20**, 452–456.
4 P. Ahuja, S. K. Ujjain and R. Kanojia, *Appl. Surf. Sci.*, 2017, **404**, 197–205.
5 W. Li and S. T. Oyama, *J. Am. Chem. Soc.*, 1998, **120**, 9047–9052.
6 S. Biswas, B. Dutta, K. Mullick, C. H. Kuo, A. S. Poyraz and S. L. Suib, *ACS Catal.*, 2015, **5**, 4394–4403.
7 L. Singoredjo, R. Korver, F. Kapteijn and J. Moulijn, *Appl. Catal., B*, 1992, **15**, 297–316.
8 A. P. E. York, J. B. Claridge, M. L. H. Green and S. C. Tsang, *Stud. Surf. Sci. Catal.*, 1994, **82**, 315–326.
9 S. K. Ghosh, *ACS Omega*, 2020, **5**, 25493–25504.
10 S. Sui, X. Wang, X. Zhou, Y. Su, S. Riffat and C. Liu, *J. Mater. Chem. A*, 2017, **5**, 1808–1825.
11 K. A. Stoerzinger, M. Risch, B. Han and Y. Shaon-Horn, *ACS Catal.*, 2015, **5**, 6021–6035.
12 C. W. Machan, *ACS Catal.*, 2020, **10**, 2640–2655.
13 O. Z. Sharaf and M. F. Orhan, *Renewable Sustainable Energy Rev.*, 2014, **32**, 810–853.

14 K. M. Naik and S. Sampath, *Electrochim. Acta*, 2018, **292**, 268–275.
15 K. M. Naik, E. Higushi and H. Inoue, *Int. J. Hydrogen Energy*, 2023, **48**, 30741–30750.
16 Z. Zhang, J. Liu, J. Gu and L. Su, *Energy Environ. Sci.*, 2014, **7**, 2535–2558.
17 C. M. A. Parlett, K. Wilson and A. F. Lee, *Chem. Soc. Rev.*, 2013, **42**, 3876–3893.
18 J. E. Van Den Reijen, P. H. Keijzer and P. E. De Jongh, *Materialia*, 2018, **4**, 423–430.
19 T. Weller, J. Timm, L. Deilmann, T. S. Doerr, C. Greve, A. S. Cherevan, P. A. Beaucage, U. B. Wiesner, E. M. Herzig, D. Eder and R. Marschall, *Small Struct.*, 2023, **4**, 2200184–2200194.
20 T. Priamushko, R. Guillet-Nicolas and F. Kleitz, *Inorganics*, 2019, **7**, 98–121.
21 T. Wang, M. Shi, S. Zhang, L. Wu, B. Jiang, J. Cai and C. Li, *Appl. Surf. Sci.*, 2020, **530**, 147304–147314.
22 E. Akbari, S. M. Alavi, M. Rezaei and A. Larimi, *Ind. Eng. Chem. Res.*, 2021, **60**, 7572–7587.
23 B. Bai, J. Li and J. Hao, *Appl. Catal., B*, 2015, **164**, 241–250.
24 M. Imperor-Clerc, D. Bazin, M. D. Appay, P. Beaunier and A. Davidson, *Chem. Mater.*, 2004, **16**, 1813–1821.
25 Y. S. Ding, X. F. Shen, S. Gomez, H. Luo, M. Aindow and S. L. Suib, *Adv. Funct. Mater.*, 2006, **16**, 549–555.
26 L. W. Finger, D. E. Cox and A. P. Jephcoat, *J. Appl. Crystallogr.*, 1994, **27**, 892–900.
27 J. F. Moulder, J. Chastain and R. C. King, *Handbook of X-Ray Photoelectron Spectroscopy: A Reference Book of Standard Spectra for Identification and Interpretation of XPS Data*, Perkin-Elmer Corp., 1995.
28 M. Stamatakis, *Zacros: advanced lattice-KMC simulation made easy*, Software code available from **https://www.zacros.org**, 2013.
29 H. Su, Y. Gorlin, I. C. Man, F. Calle-Vallejo, J. K. Norskov, T. F. Jaramillo and J. Rossmeisl, *Phys. Chem. Chem. Phys.*, 2012, **14**, 14010–14022.
30 F. Rasera, A. S. Thill, L. P. Matte, G. Z. Girotto, H. V. Casara, G. B. Della Mea, N. M. Balzaretti, F. Poletto, C. Brito and F. Bernardi, *ACS Appl. Nano Mater.*, 2023, **6**, 6435–6443.
31 G. B. Della Mea, L. P. Matte, A. S. Thill, F. O. Lobato, E. V. Benvenutti, L. T. Arenas, A. Jürgensen, R. Hergenröder, F. Poletto and F. Bernardi, *Appl. Surf. Sci.*, 2017, **422**, 1102–1112.
32 G. T. Baronetti, O. A. Scelza, A. A. Castro, V. C. Corberan and J. L. G. Fierro, *Appl. Catal.*, 1990, **61**, 311–328.
33 C. D. Wagner, D. A. Zatko and R. H. Raymond, *Anal. Chem.*, 1980, **52**, 1445–1451.
34 M. Avrami, *J. Chem. Phys.*, 1941, **9**, 177–184.
35 M. Avrami, *J. Chem. Phys.*, 1940, **8**, 212–224.
36 M. A. H. Vogt, A. S. Thill, L. P. Matte, C. Escudero and F. Bernardi, *ACS Appl. Nano Mater.*, 2023, **6**, 5712–5720.
37 A. S. Cherevan, L. Deilmann, T. Weller, D. Eder and R. Marschall, *ACS Appl. Energy Mater.*, 2018, **1**, 5787–5799.
38 M. Yang, H. Yuan, H. Wang and P. Hu, *Sci. China:Chem.*, 2018, **61**, 457–467.
39 Z. Duan and G. Wang, *J. Phys. Chem. C*, 2013, **117**, 6284–6292.